Scheimpflug Lidar for combustion diagnostics

Malmqvist, Elin; Brydegaard, Mikkel; Aldén, Marcus; Bood, Joakim

Published in:
Optics Express

DOI:
10.1364/OE.26.014842

2018

Research Article | Vol. 26, No. 12 | 11 Jun 2018 | OPTICS EXPRESS 14842
Optics EXPRESS

Scheimpflug Lidar for combustion diagnostics

ELIN MALMQVIST,[1,*] MIKKEL BRYDEGAARD,[1,2] MARCUS ALDÉN,[1] AND JOAKIM BOOD[1]

[1]*Division of Combustion Physics, Department of Physics, Lund University, Sölvegatan 14, Lund, Sweden*
[2]*Norsk Elektro Optikk Lund AB, Maskinvägen 1, Lund, Sweden*
[*]*elin.malmqvist@forbrf.lth.se*

Abstract: A portable Lidar system developed for large-scale (~1-20 m) combustion diagnostics is described and demonstrated. The system is able to perform remote backscattering measurements with range and temporal resolution. The range resolution is obtained by sharply imaging a part of the laser beam onto a CMOS-array or ICCD detector. The large focal depth required to do this is attained by placing the laser beam, the collection optics and the detector in a so-called Scheimpflug configuration. Results from simulations of the range capabilities and range resolution of the system are presented and its temporal resolution is also discussed. Various applications, important for combustion diagnostics, are also demonstrated, including Rayleigh scattering thermometry, aerosol detection and laser-induced fluorescence measurements. These measurements have been carried out using various continuous-wave GaN diode lasers, emitting in the violet-blue (405 – 450 nm) wavelength regime. It is anticipated that Scheimpflug Lidar will provide a useful and versatile diagnostic tool for combustion research, not only for fundamental studies, but in particular for applications at industrial sites.

OCIS codes: (010.3640) Lidar; (120.1740) Combustion diagnostics.

References and links

1. A. C. Eckbreth, *Laser Diagnostics for Combustion Temperature and Species* (CRC Press, 1996), Vol. 3.
2. A. Ehn, J. Zhu, X. Li, and J. Kiefer, "Advanced laser-based techniques for gas-phase diagnostics in combustion and aerospace engineering," Appl. Spectrosc. **71**(3), 341–366 (2017).
3. R. K. Hanson, R. M. Spearrin, and C. S. Goldenstein, *Spectroscopy and Optical Diagnostics of Gases* (Springer, 2016).
4. A. McIlroy, J. B. Jeffries, K. Kohse-Höinghaus, and J. B. Jeffries, "Applied Combustion Diagnostics," (2002).
5. M. Aldén, J. Bood, Z. Li, and M. Richter, "Visualization and understanding of combustion processes using spatially and temporally resolved laser diagnostic techniques," Proc. Combust. Inst. **33**(1), 69–97 (2011).
6. M. G. Allen, E. R. Furlong, and R. K. Hanson, "Tunable diode laser sensing and combustion control," in *Applied Combustion Diagnostics*, K. Kohse-Höinghaus, ed. (Taylor and Francis, 2002), pp. 479–498.
7. S. Roy, J. R. Gord, and A. K. Patnaik, "Recent advances in coherent anti-Stokes Raman scattering spectroscopy: Fundamental developments and applications in reacting flows," Pror. Energy Combust. Sci. **36**(2), 280–306 (2010).
8. R. K. Hanson, "Applications of quantitative laser sensors to kinetics, propulsion and practical energy systems," Proc. Combust. Inst. **33**(1), 1–40 (2011).
9. W. D. Kulatilaka, H. U. Stauffer, J. R. Gord, and S. Roy, "One-dimensional single-shot thermometry in flames using femtosecond-CARS line imaging," Opt. Lett. **36**(21), 4182–4184 (2011).
10. A. Bohlin and C. J. Kliewer, "Communication: Two-dimensional gas-phase coherent anti-Stokes Raman spectroscopy (2D-CARS): Simultaneous planar imaging and multiplex spectroscopy in a single laser shot," J. Chem. Phys. **138**(22), 221101 (2013).
11. M. B. Frish, R. T. Wainner, M. C. Laderer, B. D. Green, and M. G. Allen, "Standoff and miniature chemical vapor detectors based on tunable diode laser absorption spectroscopy," IEEE Sens. J. **10**(3), 639–646 (2010).
12. J. Chen, A. Hangauer, R. Strzoda, and M. C. Amann, "Laser spectroscopic oxygen sensor using diffuse reflector based optical cell and advanced signal processing," Appl. Phys. B Lasers Opt. **100**(2), 417–425 (2010).
13. Z. Wang and S. T. Sanders, "Toward single - ended absorption spectroscopy probes based on backscattering from rough surfaces : H 2 O vapor measurements near 1350 nm," Appl. Phys. B **121**(2), 187–192 (2015).
14. W. Y. Peng, C. S. Goldenstein, R. Mitchell Spearrin, J. B. Jeffries, and R. K. Hanson, "Single-ended mid-infrared laser-absorption sensor for simultaneous in situ measurements of H2O, CO2, CO, and temperature in combustion flows," Appl. Opt. **55**(33), 9347–9359 (2016).
15. C. S. Goldenstein, R. Mitchell Spearrin, and R. K. Hanson, "Fiber-coupled diode-laser sensors for calibration-

#320075 https://doi.org/10.1364/OE.26.014842
Journal © 2018 Received 19 Jan 2018; revised 21 Apr 2018; accepted 22 Apr 2018; published 29 May 2018

Optics EXPRESS

free stand-off measurements of gas temperature, pressure, and composition," Appl. Opt. **55**(3), 479–484 (2016).
16. Z. Wang, S. T. Sanders, and M. A. Robinson, "Spatially resolved concentration measurements based on backscatter absorption spectroscopy," Appl. Phys. B **122**(6), 176 (2016).
17. C. Weitkamp, ed., *Lidar: Range-Resolved Optical Remote Sensing of the Atmosphere* (Springer Science & Business, 2006), Vol. **102**.
18. B. Kaldvee, A. Ehn, J. Bood, and M. Aldén, "Development of a picosecond lidar system for large-scale combustion diagnostics," Appl. Opt. **48**(4), B65–B72 (2009).
19. B. Kaldvee, J. Bood, and M. Aldén, "Picosecond-lidar thermometry in a measurement volume surrounded by highly scattering media," Meas. Sci. Technol. **22**(12), 125302 (2011).
20. B. Kaldvee, J. Wahlqvist, M. Jonsson, C. Brackmann, B. Andersson, P. van Hees, J. Bood, and M. Alden, "Room-fire characterization using highly range-resolved picosecond Lidar diagnostics and CFD simulations," Combust. Sci. Technol. **185**(5), 749–765 (2013).
21. B. Kaldvee, C. Brackmann, M. Aldén, and J. Bood, "Highly range-resolved ammonia detection using near-field picosecond differential absorption lidar," Opt. Express **20**(18), 20688–20697 (2012).
22. T. Leffler, C. Brackmann, A. Ehn, B. Kaldvee, M. Aldén, M. Berg, and J. Bood, "Range-resolved detection of potassium chloride using picosecond differential absorption light detection and ranging," Appl. Opt. **54**(5), 1058–1064 (2015).
23. B. Kaldvee, C. Brackmann, M. Aldén, and J. Bood, "LII-lidar: Range-resolved backward picosecond laser-induced incandescence," Appl. Phys. B Lasers Opt. **115**(1), 111–121 (2014).
24. M. Brydegaard, A. Gebru, and S. Svanberg, "Super resolution laser radar with blinking atmospheric particles - Application to interacting flying insects," Prog. Electromagnetics Res. **147**, 141–151 (2014).
25. L. Mei and M. Brydegaard, "Atmospheric aerosol monitoring by an elastic Scheimpflug lidar system," Opt. Express **23**(24), A1613–A1628 (2015).
26. L. Mei and M. Brydegaard, "Development of a Scheimpflug Lidar system for atmospheric aerosol monitoring," in *EPJ Web of Conferences* (EDP Sciences, 2016), Vol. **119**, p. 27005.
27. M. Brydegaard, E. Malmqvist, S. Jansson, G. Zhao, J. Larsson, and S. Török, "The Scheimpflug Lidar method," in *SPIE Proceedings* (2017), Vol. **10406**.
28. G. Zhao, M. Ljungholm, E. Malmqvist, G. Bianco, L. A. Hansson, S. Svanberg, and M. Brydegaard, "Inelastic hyperspectral lidar for profiling aquatic ecosystems," Laser Photonics Rev. **10**(5), 807–813 (2016).
29. L. Mei and M. Brydegaard, "Continuous-wave differential absorption lidar," Laser Photonics Rev. **9**(6), 629–636 (2015).
30. J. Carpentier, "Improvements in enlarging or like cameras," GB Pat. No.1139 (1901).
31. T. Scheimpflug, "Improved method and apparatus for the systematic alteration or distortion of plane pictures and images by means of lenses and mirrors for photography and for other purposes," GB Pat. No.1196 (1904).
32. H. M. Merklinger, *Focusing the View Camera* (2010), Vol. 0.
33. F. Migliorini, S. De Iuliis, F. Cignoli, and G. Zizak, "How "flat" is the rich premixed flame produced by your McKenna burner?" Combust. Flame **153**(3), 384–393 (2008).
34. F. Vestin, M. Afzelius, C. Brackmann, and P. E. Bengtsson, "Dual-broadband rotational CARS thermometry in the product gas of hydrocarbon flames," Proc. Combust. Inst. **30**(1), 1673–1680 (2005).
35. F.-Q. Zhao and H. Hiroyasu, "The applications of laser Rayleigh scattering to combustion diagnostics," Pror. Energy Combust. Sci. **19**(6), 447–485 (1993).
36. T. Leffler, C. Brackmann, W. Weng, Q. Gao, M. Aldén, and Z. Li, "Experimental investigations of potassium chemistry in premixed flames," Fuel **203**, 802–810 (2017).
37. J. Borggren, W. Weng, A. Hosseinnia, P.-E. Bengtsson, M. Aldén, and Z. Li, "Diode laser-based thermometry using two-line atomic fluorescence of indium and gallium," Appl. Phys. B Lasers Opt. **123**(12), 278 (2017).

1. Introduction

Measurements of parameters such as species concentration, temperature, and velocity, are of utmost importance for optimization of combustion processes in terms of efficiency and emission of air pollutants. Laser diagnostic techniques have for a long time proven to be very valuable tools for such measurements, often providing non-intrusive in situ measurements with high spatial and temporal resolution. Comprehensive reviews of laser-spectroscopic techniques for combustion diagnostics, including a wealth of application examples, are given in [1–5] and references therein.

Although a number of laser-based techniques are sufficiently mature and robust to be employed in industrial environments, most of them require ports at multiple angles for optical access, the detection range is relatively short (typically on the order of centimeters), and both laser and detection equipment need to be located in close proximity to the measurement object. These limitations prevent diagnostics in for example large-scale boilers, power plants and fires. Line-of-sight absorption methods [6] or techniques with highly directional signal emission, such as coherent anti-Stokes Raman spectroscopy (CARS) [7] can be performed

Optics EXPRESS

with relatively small optical access, but typically two opposing optical ports are needed. Concepts based on absorption spectroscopy, where the signal is integrated along the line of sight, are ideally suited for applications in environments where the temperature, pressure, and gas composition have uniform distributions [8]. However, since many industrial combustion processes often implies strongly inhomogeneous measurement volumes, line-of-sight absorption techniques are often not sufficient. Although measurements of average concentrations along the line of sight are possible, quantification of the data is significantly more difficult, resulting in higher uncertainty, particularly if the temperature varies substantially. In terms of CARS, industrial demonstrations have so far been restricted to point measurements, see [7] and references therein, although one-dimensional (1-D) [9] and two-dimensional (2-D) CARS measurements have been demonstrated [10].

Hence, for diagnostics in full-scale industrial devices, often possessing intractable physical and optical access, single-ended techniques able to probe over large distances, yet providing high spatial and temporal resolution, are desired. Recently major efforts have been directed towards development of single-ended absorption sensors based on reflection off a surface, diffuse or smooth, either naturally present in the device under study or incorporated during the experiment. Although simultaneous measurements of multiple species and temperature have been demonstrated [11–16], the sensors do not provide spatial resolution along the laser beam.

Light detection and ranging, Lidar, also referred to as laser-radar, is a remote sensing technique that can provide range resolved measurements over very long distances (up to ~100 km). It is a well-established technique in for example atmospheric research, where it typically is employed to study aerosols, clouds, molecular constituents, wind speed, and temperature [17]. Conventionally, range resolution is obtained by temporally resolving the backscattered radiation, i.e. through time-of-flight detection. The achievable range resolution is dependent on the laser pulse duration, bandwidth and sampling rate of the receiver electronics, and signal-to-noise ratio. In order to provide adequate range resolution for combustion diagnostics, ultrashort (picosecond or shorter) laser pulses together with a detection system that is fast enough to match the laser pulse duration are required. Furthermore, in order to obtain adequate signal-to-noise ratio, particularly in single-shot measurements, which are necessary in turbulent flames, high enough pulse energy is required. Special care therefore has to be taken in terms of using optics that can tolerate the high laser peak powers delivered by high-power ultrashort lasers.

Our group has previously demonstrated a range resolution of 5 mm with a Lidar system based on picosecond laser pulses and ultrafast detection using a streak camera [18]. We also demonstrated various combustion diagnostics with ps-Lidar, such as Rayleigh thermometry in flames [18], oven [19], and full-scale room fire experiment [20], quantitative species concentration measurements based on differential absorption Lidar (DIAL) [21,22], and measurements of soot volume fractions in flames [23]. Utilizing the temporal shape of the backward-emitted radiation to achieve range resolution basically requires that the light-matter interaction process generating the signal of interest occurs on a time scale comparable with the laser pulse duration or shorter. This requirement makes it difficult to use laser-induced fluorescence (LIF) with ps-Lidar in combustion environments, since typical fluorescence lifetimes are on the nanosecond scale, resulting in a range resolution on the decimeter to meter scale. Although this problem can in principle be circumvented if the recorded signal is deconvoluted with the fluorescence decay curve, this is generally not a viable approach since the fluorescence lifetime usually is unknown and varies in time and space along the measurement path.

In the present paper we demonstrate a new Lidar approach for combustion diagnostics based on a Continues-Wave (CW) laser and the Scheimpflug principle. In Scheimpflug-Lidar [24–29], range resolution is achieved through triangulation, rather than the time-of-flight detection as in traditional Lidar. By arranging a detector array, collection optics, and the laser

Optics EXPRESS

beam in a configuration that fulfils the Scheimpflug condition, infinite focal depth can be obtained along the laser beam and it can thus be sharply imaged onto the detector array. Since range resolution in this Lidar configuration is achieved by imaging the laser-induced emission, instead of utilizing time-resolved detection, the setup can be rescaled to cover fine details without the need of ultrashort laser pulses and issues with high peak powers. In addition, LIF is fully applicable with this approach. Thus, Scheimpflug Lidar opens up for range-resolved single-ended diagnostics with setups based on small inexpensive diode lasers, which may reduce the size, weight, and cost of the system, thereby also facilitating its mobility.

The paper is structured as follows: Following this introduction, Section 2 describes the Scheimpflug principle and the expected capacity of the system is predicted through simulations of coverable range and spatial resolution. The experimental arrangement is outlined in Section 3. In section 4, results showing the general features and capacity of the Scheimpflug Lidar setup are presented, followed by results illustrating the resolution of the system. After that, Rayleigh scattering thermometry in a non-sooty flame is demonstrated as well as LIF measurements in an indium seeded flame. The paper ends with conclusions and outlook in Section 5.

2. Scheimpflug principle

The Scheimpflug principle [30,31] is an optical principle that describes how the focal plane of, for example, a camera can be shifted by titling the lens in relation to the detector and thereby achieve a large focal depth. This concept is illustrated in Fig. 1 with three simulated images of a railway track taken from a moving train. Figure 1(a) illustrates the case of a conventional camera. In a conventional camera, the front and back focal planes are parallel to the detector and lens planes, and it is strictly the volume in between these two focal planes that is in focus. Consequently, only a part of the tracks stretching towards the horizon is in focus. The conventional camera case does not suffer from motion blur since the required exposure time is short due to a large aperture. One possible way to achieve a larger focal depth with a conventional setup is to use a small aperture, such as a pinhole. It is then possible to gain infinite focal depth, but at the expense of very low light collection efficiency, requiring long exposure times, which makes the system subject to motion blur. This is illustrated in Fig. 1(b), where focus has been achieved along the tracks but the movement of the train causes blurring. If instead a large aperture is used and the lens plane is tilted in relation to the detector, according to the Scheimpflug principle, the focal plane can coincide with the rails and infinite focal depth can be obtained without reducing the efficiency of the light collection. The result can be seen in Fig. 1(c) where focus has been achieved along the tracks to infinity without any motion blur. The large focal depth is only achieved in the plane that lies along the train tracks. Features extruding from this plane, such as the tree tops, will be out of focus.

To achieve focus along a specific object plane with a Scheimpflug setup, the detector and collection lens have to be aligned in such a way that their associated planes intersect the object plane along the same line (the Scheimpflug intersection), as illustrated in Fig. 2. However, the Scheimpflug rule alone does not ensure focus along one specific plane, since the image plane and the lens plane together can be rotated around the Scheimpflug intersection. The position of the object plane is further constrained by the Hinge rule, which states that the front focal plane and the plane parallel with the detector that intersects the center of the lens must intersect the laser beam along one line (the Hinge intersection). If the distance between the detector and the lens planes is changed the plane of focus will hinge around the Hinge intersection [32].

Optics EXPRESS

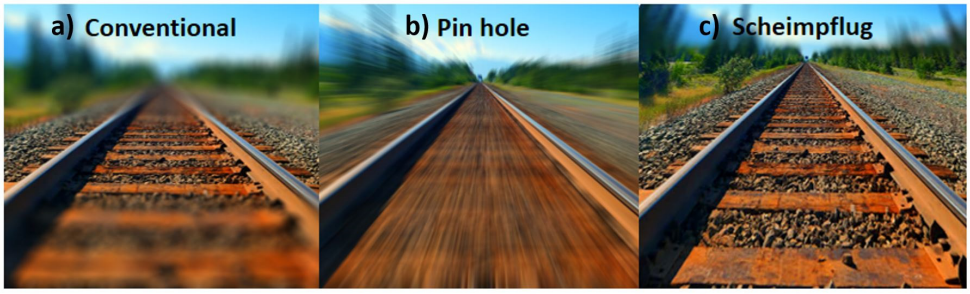

Fig. 1. Images of railway tracks stretching to the horizon, taken from a moving train with different camera setups. The effects of the different setups have been simulated for the sake of clarity. In (a) an image from a conventional camera is shown, where the focal depth is limited. (b) shows the corresponding image taken with a small aperture, or pin hole. Infinite focal depth can then be obtained, but the long exposure time needed causes motion blur. (c) is taken with a Scheimpflug configuration, i.e. with a large aperture and the lens tilted in relation to the detector. Focus is attained up to infinity without any motion blurring. Behind the optical infinity (horizon) the focus is lost again.

In Scheimpflug Lidar, a laser beam transmitted through the volume of interest is placed along the object plane and the backscattering from the beam is sharply imaged onto a detector placed along the image plane. Equation (1) gives the observed range (z_n) of a specific position (p_n) of pixel n on the detector for a Scheimpflug Lidar setup. It was obtained by using the trigonometrical constraints given by the Scheimpflug and Hinge intersections [see Fig. 2]. The variables of Eqs. (1)-(3) are defined according to Fig. 2, thus z_n is range, L is length of the detector, f is the focal length of the lens, b_c is the distance between the center of the receiving lens and the center of the detector, α is the angle between the lens plane and the detector plane. ϕ is the angle between the lens plane and the laser beam plane, p_n is the position of pixel n on the detector, n is the pixel number and l_{pix} is the width/pitch of a pixel.

$$z_n = \frac{f \cdot \sin(\pi - \alpha - \Phi)}{\sin(\alpha) \cdot \tan\left(\frac{\pi}{2} + \arctan\left(\frac{p_n \cdot \cos(\alpha)}{b_c + p_n \cdot \sin(\alpha)}\right) - \Phi\right)} \tag{1}$$

$$\phi = \arctan\left(\frac{f \cdot \tan(\alpha)}{b_c - f}\right) \tag{2}$$

$$p_n = n \cdot l_{pix} - L/2 \tag{3}$$

There are two unknown variables in Eq. (1), b_c and z_n. The signal from a reference target distance, z_{ref}, that ends up in a pixel with pixel number, n_{ref}, may be used to obtain b_c for the specific Scheimpflug setup. This b_c can then be used to calculate z_n for all n.

The theoretical range resolution of Scheimpflug Lidar is thus constrained by the angles at which the pixels are observing the laser beam (govern by the Scheimpflug/Hinge conditions) as well as by the width of the pixels. Due to the nature of the triangulation used to obtain range information, i.e. a specific angle represents a specific range, the range resolution of Scheimpflug-Lidar is non-linear. The pixels at far ranges observe a more extended volume than the pixels at near ranges. Figure 3 displays theoretical range curves and corresponding range resolution for five different configurations with the current system based on the array detector, (f = 200 mm, L = 28 mm).

Optics EXPRESS

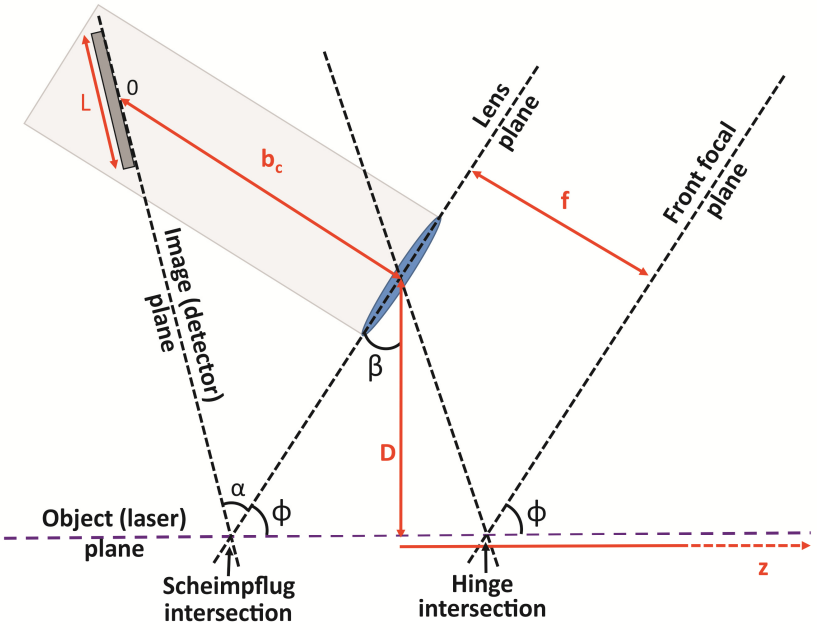

Fig. 2. A schematic figure of a Scheimpflug Lidar setup. All the necessary angles and distances needed for calculation of range and resolution can be seen in the figure. The relevant planes are marked with dotted lines, and the distances are marked with red arrows. The Scheimpflug and Hinge intersection are shown in the lower part of the figure. The distance D (base line) defines the perpendicular distance between the laser beam and the center of the lens. β defines the angle between the lens plane and the plane of D. Both D and β are discussed further below.

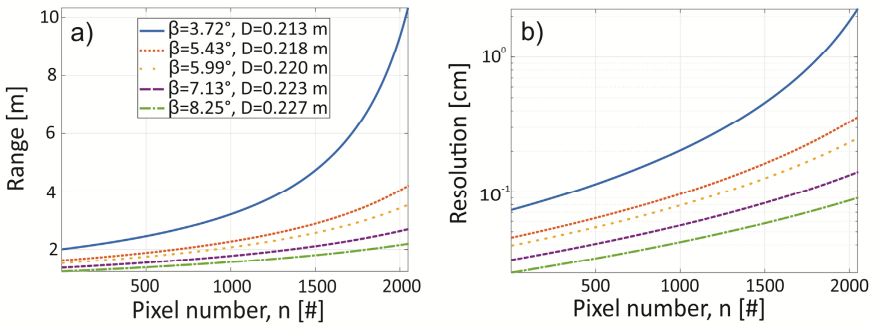

Fig. 3. (a) Analytical range curves and (b) the corresponding resolution curves for five different Scheimpflug configurations. The resolution curves in (b) is on logarithmic scale. The angle β (tilt of lens) and the distance D are defined in Fig. 2.

An important factor to consider in combustion diagnostics is the actual distance between the laser transmitter and receiver (the baseline) since this determines the required size of the optical access. This distance [D, defined in Fig. 2] varies with f. A longer f will result in a higher angular resolution and thereby higher range resolution, but also a larger distance, D, while a case with a shorter f will give shorter distance D, but at the expense of lower range resolution for the same range interval. Figures 4(a)-4(c) displays the calculated far limit (red) and near limit (blue) range for different D and three different f (200 mm, 100 mm, 50 mm) for our system when a linear CMOS array with a detector length of 2.8 cm is used. The maximum range value for the smallest D was set to ~12 m for all three cases. Figures 4(d)-4(f) displays the corresponding far limit (black) and near limit (green) range resolution. The

Optics EXPRESS

distance D for the three cases is ~22 cm, ~11.5 cm and ~6.3 cm, respectively. Consequently, the focal length, f, of the collection optics should be chosen according to the current application, e.g. if the optical access is small, a short f can be used, but the covered range interval will be small if high range resolution is required.

It is also important to point out that the size of the optical access is not necessarily limited by the baseline separation, D. The system could be placed at a distance from the optical access, which will make the required size smaller. The ideal case would be to place the system at a distance to the optical access which places the minimum detectable range (which is always at a range offset from the position of the system) at the start of the probe volume. The whole probe volume can thus be monitored while the required size of the opening would be smaller than the case where the system is right next to the optical access. Another way to improve on the covered range interval would be to use a detector with a longer chip.

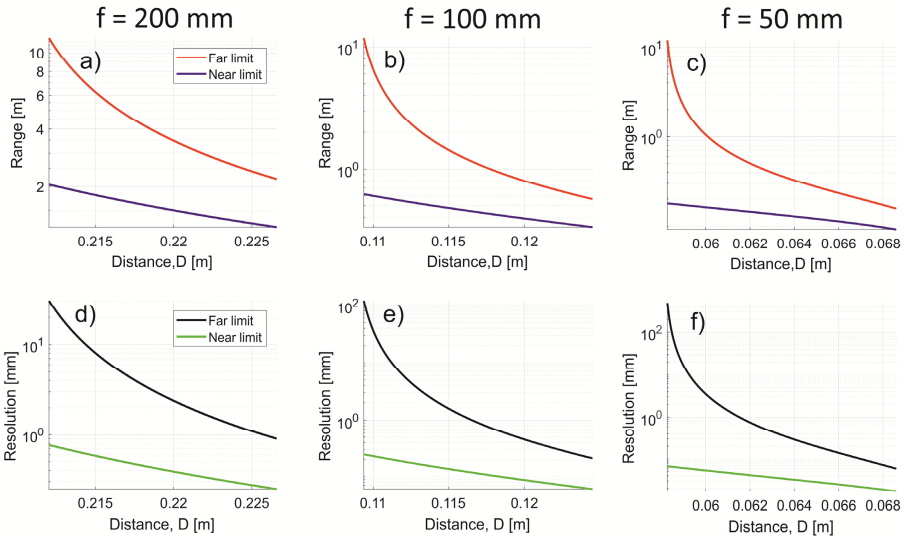

Fig. 4. Obtained far limit and near limit range versus different distances, D (Fig. 2) for (a) f = 200 mm (b) f = 100 mm (c) 50 mm, with a line scan detector with a length of 28 mm (1x2048 pixels). (c)-(d) The corresponding maximum and minimum resolution. For a fixed f, it may be seen that a case where a large range interval is monitored gives much worse range resolution (here represented by the pixel foot print) than a case where a short range interval is monitored. A small f, leads to a small distance D, but also low range resolution for large range intervals. A large f, on the other hand, results in a larger distance D, but better resolution for larger range intervals. The setup utilized in this work has a focal length of 200 mm (corresponding to panel a), which means that D was around 22 cm.

In Fig. 3, the laser beam was considered infinitely narrow and in this case the resolution of Scheimpflug Lidar is only constrained by the trigonometrical principles of the Scheimpflug and Hinge intersections. However, in reality the beam will always have a finite width since an infinitely narrow beam cannot be implemented due to the diffraction of light. The finite width of the laser beam will affect the resolution of Scheimpflug Lidar. As can be seen in Fig. 5, a finite beam width, defined by the light blue area, means that the footprints of adjacent pixels will overlap in the range direction inside the beam. Thus, the resolution curves shown in Fig. 3(b) only hold true for a beam that is infinitely narrow, seen as the dark blue line at the center of the wide laser beam in Fig. 5. In order to calculate resolution curves corresponding to measurements with a beam of a finite width, a custom-made ray tracing script simulating backscattering from a 3D beam with a Gaussian cross section was created. In this program, the defined beam is divided into volume cubes [represented by the dots in Fig. 5] and the overlap between the footprints of the detector pixels and the volume cubes in the beam is used

Optics EXPRESS

to achieve a sensitivity profile over range. This is illustrated in the lower part of Fig. 5 where the number of volume cubes overlapped by the pixel footprint is plotted as a function of range. The area below this function corresponds to the range dependent sensitivity curve in the pixel and its full width at half maximum (FWHM) defines the range resolution. In the simulation, random noise has been added to the spatial coordinates of the volume cubes as a way to avoid beating between the discretized volume cubes and the discretized detector pixels. Further details about the simulation program is discussed in [27]. Figure 6 displays resolution curves corresponding to the same cases as in Fig. 3, but here based on the simulation program assuming a laser beam of finite width (FWHM: 0.2, 1.6, 3.4 mm). For these simulations the beam was considered to be collimated throughout the probe volume. The simulated resolution curves clearly demonstrate how the resolution degrades with increasing width of the laser beam for all the different Scheimpflug configurations. This highlights the importance of keeping the width of the laser beam narrow if high resolution is required.

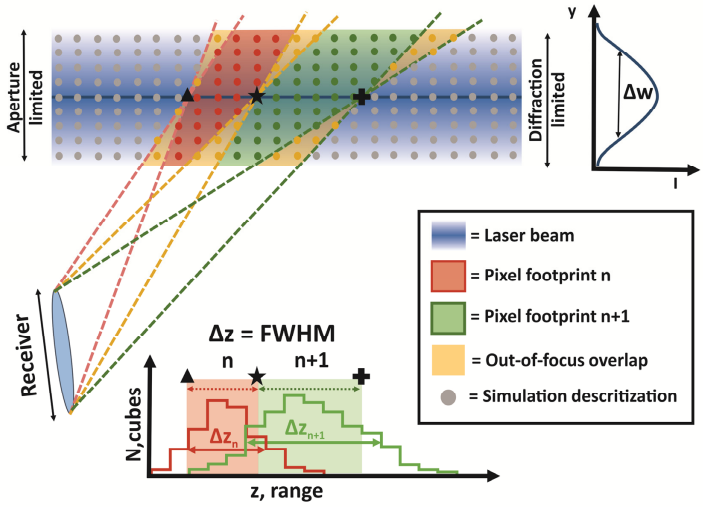

Fig. 5. An illustration of the principles of the Scheimpflug Lidar simulation program. The program calculates the range, resolution and signal strength for beams of different widths and shapes. The top part of the figure shows the laser beam (blue area) which is divided up into discrete volume cubes represented by dots. The volumes that two adjacent pixel observe are represented by a red and a green area and their out-of-focus overlap inside the beam is marked with yellow. The plots at lower part of the figure shows how many volume cubes the foot print of a pixel overlap at each range. The FWHM of a distribution defines the resolution in the corresponding pixel and its area corresponds to the pixel signal strength. When the beam has a finite width, the two foot prints overlap in range inside the laser beam. The signal in each pixel gets smeared out in the range direction and starts to overlap with the signal in adjacent pixels. When the laser beam is infinitely narrow, represented here by the thick, dark blue center line, the two pixel footprints do not overlap in range inside the laser beam, as seen by the red and green shaded boxes in the plot. The spread of the signal in range thus corresponds only to the size of the pixel in question's footprint, determined by the Scheimpflug principle.

Optics EXPRESS

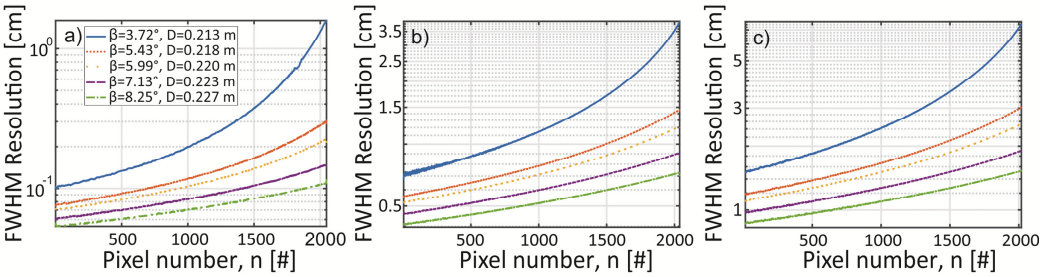

Fig. 6. Simulated practical resolution for the same ranges as in Fig. 3 with a beam with a Gaussian beam profile with FWHM of (a) 0.2 mm, (b) 1.6 mm (c) 3.4 mm. The resolution scale is logarithmic.

3. Experimental setup

The experimental setup is presented in Fig. 7. A laser beam is transmitted through the region-of-interest, e.g. a flame above a burner, and a detector with a collection lens in front is aligned so that sharp focus is achieved along the laser beam. Scattering or fluorescence induced by the laser beam is thus imaged onto the detector according to the Scheimpflug principle. The laser beam is terminated in a black beam dump. Various continuous-wave diode lasers have been utilized in this setup, both inexpensive, multimode, high-power diode lasers and more advanced single-mode lasers of lower power, as summarized in Table 1. A line-scan detector with high readout rate (max 4000 Hz) was used for most of the measurements presented here, but two ICCD cameras (PI-MAX4, PI-MAX2) were used for the fluorescence measurements as a way to also demonstrate the 2D-imaging capacity of the Lidar technique. The specifications of the three detectors can be seen in Table 2. The signal is collected with a 50.8-mm diameter spherical lens (f = 200 mm) and a suitable band-pass filter is used in front of the detector to suppress background radiation. To achieve Scheimpflug configuration, a wedge is used to tilt the detector in relation to the lens, and the whole detection arrangement is placed on a mount which can be rotated around the vertical and side-to-side axes for the purpose of overlapping beam and field-of-view. The distance between the camera and the transmitted laser beam [D in Fig. 2] was between 21.5 and 22.5 cm in all measurements reported here. This distance is constrained by the Scheimpflug and hinge rules and it will thus change depending on the focal length of the lens and the desired range interval.

The kHz-sampling rate of the line scan camera enables online background subtraction during measurements by modulating the laser beam on and off in synchronization with the camera exposures, see e.g [25]. A Johnson counter is used to establish this modulation. The Johnson counter has three positions, “laser off”, “laser on”, and “reset counter”, and the trigger pulses, which are sent out from the camera during each exposure, are used to move the count between these three positions. Online background subtraction was utilized during some of the measurements presented here.

Optics EXPRESS

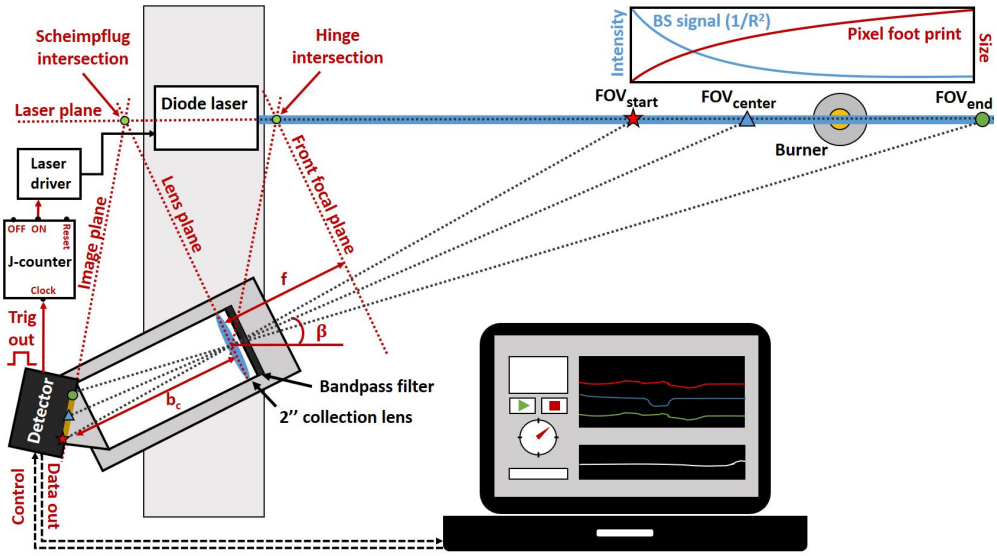

Fig. 7. A schematic of the current Lidar setup. How a counter can be incorporated in the set up to enable online background subtraction is shown to the left in the figure. The plot at the upper right corner, shows how the backscatter signal decreases with distance (blue curve) but the volume each pixel monitors, i.e. its footprint, increases with distance (red curve). This means that if the medium that is being studied has a homogenous distribution in range these two functions will to some degree cancel each other and give a flatter signal. The dynamic range of the detector can thus be utilized more efficiently over the range compared to time-of-flight Lidar.

Table 1. Specifications of the lasers utilized in the present work.

Laser manufacturer	Wavelength (nm)	Output power (mW)	Longitudinal mode
O-like	448	3000	multimode
O-like	405	500	multimode
Toptica	410	12	single mode
Toptica	451	12	single mode

Table 2. Specification of the detectors utilized in the present work.

	Linear array camera	ICCD camera 1	ICCD camera 2
Manufacturer	Synertronics Designs	Princeton Instruments	Princeton Instruments
Model	Glaz-S	PI-MAX4	PI-MAX2
Sensor type	CMOS	Intensified CCD	Intensified CCD
Chip size (pixels)	1 × 2048	1024 × 1024	1024 × 1024
Pixel size (µm)	200 × 14	13.0 × 13.0	12.8 × 12.8
Sensitive range (nm)	280-1000	350-950	200-700
Max readout rate (fps)	4000	7.7*	4*
Dynamic range	16-bit	16-bit	16-bit

*Refers to a configuration with no binning.

4. Results and discussion

4.1 Features and capacity of the Scheimpflug Lidar

The key feature of Scheimpflug Lidar is that it can provide range resolved, stand-off, measurements over large distances in the backward direction. Large probe volumes, or

Optics EXPRESS

measurement objects separated in space can thus be studied simultaneously with the technique. The dynamics of a large probe volume may also be monitored with high temporal resolution if a detector with high sampling rate is utilized in the setup. To illustrate these basic features, inherent of the technique, measurements on some highly scattering probe volumes have been carried out. Figure 8 displays two examples of data acquired by the Lidar system using the linear array detector, i.e. time-range files. Each vertical line in the time-range file corresponds to one exposure of the linear array detector. In the time-range file in Fig. 8(a) the elastic backscattering of two highly sooting flames, placed in the laser transect at different ranges (230 and 352 cm), are monitored. The measurements covered a range from 187 to 530 cm. The sampling rate of the detector was 2 kHz, giving an effective sampling rate of 1 kHz since the laser was turned off during every second exposure to enable online background subtraction. The integration time was 400 µs. A plot of the mean intensity over the time window at each range is shown. The two candles, separated in space, give rise to peaks at 230 and 352 cm, while the strongest peak at around 580 cm stems from the beam dump for termination of the laser beam. A more detailed view of the signal from one of the flames, marked with the dashed rectangle, can be seen in the insert below the time-range plot. The flickering of the flame is clearly observed, demonstrating the capacity of the Scheimpflug Lidar to resolve flame instabilities simultaneously in time and space. Figure 8(b) shows a similar time-range file in which a smoke plume, originating at a range of 352 cm, is monitored while it is dispersing along the laser transect, showing the ability of the system to study dynamics over longer distances. The effective sampling rate of the detector was 100 Hz and the integration time was 9.8 ms.

The laser used during both measurements emits at a wavelength of 405 nm. A bandpass filter with a center wavelength of 405 nm and a transmission window of 10 nm (FWHM) was used in front of the detector to suppress background radiation.

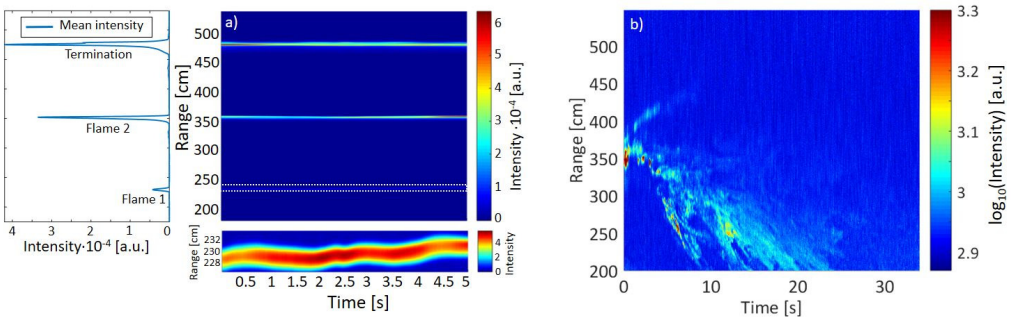

Fig. 8. (a) Time-range maps over a 5-second time window with a range interval of approximately 187 – 530 cm. Two heavily sooting flames, one located at a range of 230 cm and the other at 352 cm, were place in the Lidar transect. The data was collected with a 1 kHz effective sample rate and a 400 µs integration time. The mean intensity over the time window for each range is shown to the left. The insert in the lower panel shows a closer view of the signal from one of the flames, marked by a dotted rectangle. (b) Time-range plot displaying the spatio-temporal dynamics of smoke dispersing along the same Lidar transect during 35 seconds. The sampling rate during this measurement was 100 Hz. The intensity scale in this figure is in log scale.

4.2 Resolution

In this section, some measurements investigating the resolution of the Lidar system are presented. For these measurements a flat flame on a porous-plug McKenna burner was used. The flame was a methane/air flame with equivalence ratio 1.0. The diameter of the porous plug on the burner is 6.4 cm. During the measurements, a 5 l/min co-flow of nitrogen was used at the edge of the flame. The laser utilized for these measurements has an emission wavelength of 445 nm and a maximum output power of 3 W, with effective output of 1-1.5

Optics EXPRESS

W. A bandpass filter with center wavelength 443 nm and a FWHM of 10 nm was used to suppress background radiation. The laser beam was at a 5 mm height above the burner (HAB). The line-array detector was used and its sampling rate was 3500 Hz, giving an effective sampling rate of 1.75 kHz, due to online background subtraction. The exposure time was 266 µs. The total range covered by these measurements was ~160-420 cm.

Elastic backscattering measurements with the flat flame placed in the laser transect, was carried out. The results [see Figs. 9 and 10(a)] show a lower signal at ranges inside the flames since the intensity of Rayleigh scattering is proportional to the number density of molecules, which in turn is inversely proportional to temperature. For each measurement in the flame, a reference measurement was also recorded with only air flowing through the porous plug of the burner.

The achievable time resolution of our system depends on the time scales of the measurement volume in questions and on the required signal-to-noise ratio. The maximum temporal resolution achievable with the current line-array detector is 500 µs (exposure time of 230 µs) when online background subtraction is utilized. This corresponds to an effective sampling rate of 2 kHz. Figure 9 shows the median elastic backscattering signal for the McKenna flame for different numbers of exposures at an effective sampling rate of 1.75 kHz. Although Rayleigh scattering measurements results in fairly low signals, we get a clear signal dip at the position of the flame. If a higher signal-to-noise ratio (SNR) is desired, more averaging is required at the expense of temporal resolution. Alternatively, a lower sampling rate and longer exposure time can be used, which increases the SNR. For measurements in highly scattering environments, e.g. the sooting flames reported on in Fig. 8(a), the full temporal resolution of the system may be utilized.

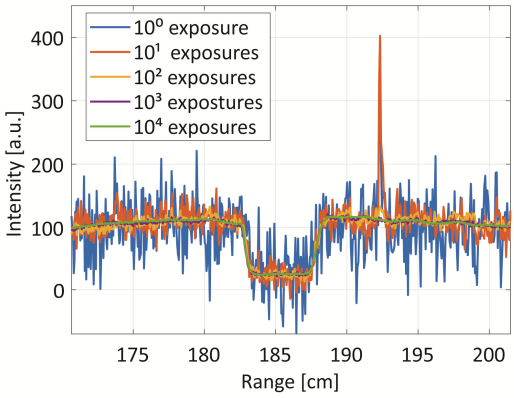

Fig. 9. Elastic Lidar signals with a flat methane/air flame placed at a range of 185 cm. The effective sampling rate of the detector was 1.75 kHz and the integration time for an exposure was 266 µs. Each curve represents the signal obtained by taking the median of a specific number of exposures in the obtained time-range file. The high peak at 192.3 cm in the blue and red curves is due to dust particles in the air surrounding the burner, which is not averaged out for low number of exposures.

To investigate the effect of the beam width on the range resolution, the width of the beam at the first edge of the McKenna burner (183 cm) was changed by shifting the position of the laser beam focus. The width of the beam was measured by moving a knife edge perpendicular to the propagation direction of the beam to cut off more and more of the beam, while the power after the knife edge was detected with a power meter. The width of the laser profile was then extracted from the resulting curve. The range position of the knife edge is indicated with a black dashed line in Figs. 10 and 11. Rayleigh scattering measurements, i.e. one measurement with the flame on and one with only air flowing through the burner, were performed for each beam width. Figure 10(a) displays the median signals from one of these

Optics EXPRESS

measurements and Fig. 10(b) shows the resulting ratio between the curves. The 10-90% slope width of the ratio curve at 183 cm, indicated in Fig. 10(b), was determined.

Normalized ratio curves for five different laser beam widths are shown in Fig. 11(a). It is clear from the figure that a decrease in beam width results in a steeper slope of the signal. The slope widths corresponding to the different beam widths are plotted in Fig. 11(b). Corresponding slope widths, simulated for each beam width, are also indicated in the figure. These were obtained by approximating the temperature profile of the flame with a top-hat function and then convoluting it with a Gaussian function with a FWHM attained from the simulated resolution at the specific range and beam width. The experimental and simulated slope widths show similar trends; a wider beam gives lower resolution. The experimental slope widths are somewhat larger than the simulated ones which can partly be explained by the laser beam profile, which is not perfectly Gaussian and has some imperfections. The experimental slope widths also show a non-linear behavior for small beam widths. This is expected as the width of the temperature gradient present at the edge of the flame becomes the limiting factor for small beam widths. The offset at zero beam width for the experimental points indicates that the width of the temperature gradient is around 5 mm [shown by the dashed horizontal yellow line in Fig. 11(b)], which agrees well with temperature profiles reported previously [33]. The simulated points, on the other hand, show a linear dependence for all beam widths since the vertical temperature profile of the burner was approximated by a top-hat function.

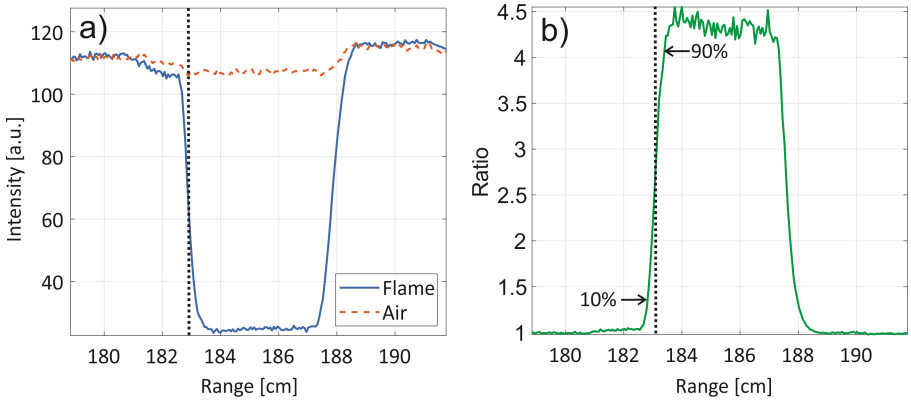

Fig. 10. (a) Median elastic Lidar signals over an 8.6 s time-window (15000 exposures). The blue curve displays the signal with a flat methane/air flame placed at a range of 185 cm and the red, dashed curve shows the reference signal acquired with only air flowing through the burner. The laser beam was at an HAB of 5 mm. The reason for the small decrease in the air signal above the burner is due to the removal of large particles by the air flow. (b) The ratio between the two curves shown in (a). The difference in range between the 10% and 90% points on the curves defines the slope width. These points are marked with arrows. The vertical dotted line indicates the position of the knife edge when the width of the beam was measured.

Optics EXPRESS

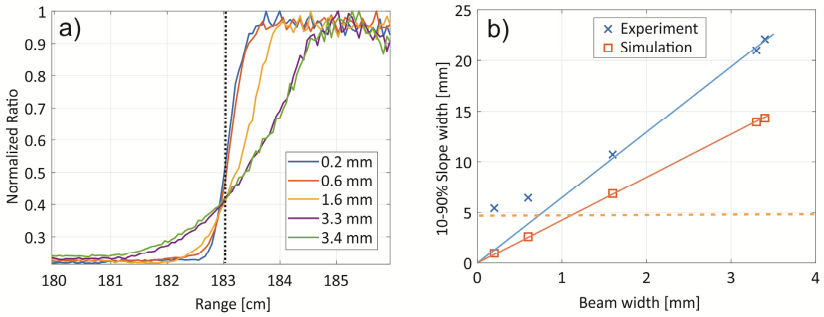

Fig. 11. (a) Normalized Rayleigh scattering ratios from the edge of a McKenna flame [see Fig. 10] for 5 different beam widths. The beam widths have been measured at the range indicated by the vertical dotted line. (b) The experimental and simulated slope widths of the ratio signal at the edge of the McKenna burner for the different beam widths. The red solid line is a linear fit to the simulated points, while the blue solid line is a linear fit to the last three experimental points. The non-linear behavior of the experimental points at small beam widths can be explained by the influence of the finite temperature gradient present at the edge of the flame. The offset of the experimental points at zero beam width indicates that the width of the temperature gradient is around 5 mm, shown by the horizontal yellow dashed line.

4.3 Rayleigh scattering thermometry in non-sooty flames

The McKenna burner was used to demonstrate Rayleigh scattering thermometry in a slightly fuel-lean ($\phi = 0.9$), premixed methane/air flame. The laser used here was the same as the one used in the measurements discussed in section 4.1-4.2. The laser beam was at 10 mm HAB and the effective sampling rate was 100 Hz. The Lidar curve recorded through the flame can be seen in Fig. 12(a) as the blue dashed curve. For reference, a corresponding Lidar curve was recorded with only room-temperature air flowing through the burner, which can be seen as the red curve in the figure. Using these curves, the flame temperature can be determined using Eq. (4),

$$T_{product} = \frac{\sigma_{product} \cdot I_{air}}{\sigma_{air} \cdot I_{product}} \cdot T_{air} \tag{4}$$

where $\sigma_{product}$ and σ_{air} are the Rayleigh cross sections of the product gas and air, respectively. The product Rayleigh cross section is the sum of the cross sections of the product species in the flame weighted with their relative abundance. $I_{product}$ and I_{air} are the measured signal intensities measured in the flame and in the room-temperature air, respectively. T_{air} is the air temperature at 295 K.

The extracted temperature curve can be seen in Fig. 12(b). The temperature is found to be about 1600 K in the product zone. Thermometry with CARS, performed in a C_2H_4/air flame 8.5 mm above the McKenna burner surface, indicated a temperature of 1700 K for a stoichiometric fuel/air mixture [34]. Despite that slightly different hydrocarbon fuels were used, with a 240 K higher adiabatic flame temperature for C_2H_4 than CH_4, the cooling by the burner surface is expected to be similar, and we therefore assess our result to be accurate within ± 100 K. The major uncertainty in our measurement is most likely due to stray light interference, but also, to some extent, due to difficulties in preventing dust particles from entering into the probe volume during the reference measurements in room-temperature air. It is important to note that these issues are not inherent in the Lidar concept, but, rather, well-known general limitations of Rayleigh scattering thermometry [35]. In fact, when no effort is made to suppress the amount of stray light, Rayleigh scattering measurements carried out from the side display a similar problem with stray light as the Lidar measurements. This might not always be the case though, since the amount of stray light interference is determined by the specific experimental geometry used. One common way to deal with stray

Optics EXPRESS

light interference in conventional Rayleigh scattering thermometry, where a 2-D camera is utilized, is to subtract the scattering signal found in pixels that are not imaging the laser beam. This method can also be applied in Lidar measurements if a 2D camera is utilized.

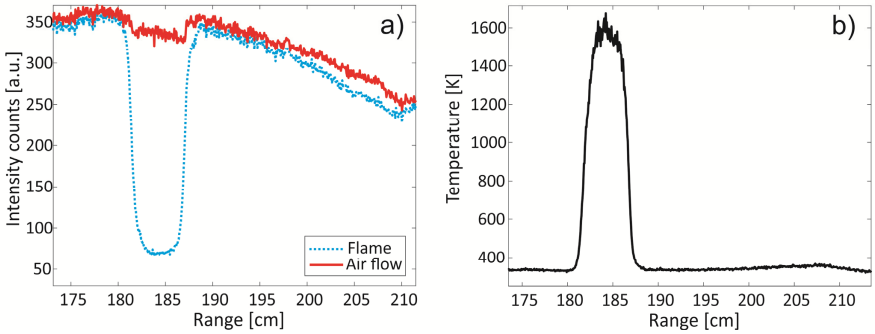

Fig. 12. (a) Median Lidar curves over a 10s-time window (1000 exposures), corresponding to molecular Rayleigh scattering with (blue) and without (red) a methane/air (with an equivalence ratio of 0.9) flame from a McKenna burner placed in the Lidar transect. The effective sampling rate was 100 Hz. The laser beam was approximately 10 mm above the burner. The slightly lower intensity above the burner for the air signal is because the air flow removes large particles from the volume. (b) The evaluated range-resolved temperature profile.

4.4 Fluorescence Lidar measurements

As previously mentioned, LIF is practically non-applicable with time-of-flight Lidar for combustion diagnostics, due to the finite fluorescence lifetime. Scheimpflug Lidar does not suffer from this limitation, since imaging is used to attain range information. As a first demonstration of fluorescence Lidar measurements in combustion using Scheimpflug Lidar, indium fluorescence from a flat methane/air flame, seeded with indium salt ($InCl_3$), was studied. The burner was a modified atomic absorption burner (Perkin-Elmer) [36] with a stabilizer plate at the top of the flame. The burner has a seeding system which enables seeding of salt solutions into the flame. The porous plug of the burner is 23 mm in diameter. A tunable, single-mode diode laser was used to excite indium through the transition $6^2S_{1/2} \leftarrow 5^2P_{1/2}$ at 410.2 nm. The laser beam was aligned above the burner, located at a distance of about 1.5 m. A PI-MAX4 intensified CCD camera, placed in a Scheimpflug configuration with a 2-inch diameter achromatic lens, collected and detected the fluorescence signal in the $6^2S_{1/2} \leftarrow 5^2P_{3/2}$ band at 451.17 nm. A bandpass filter with a center wavelength at 450 nm and spectral width of 10 nm was placed in front of the camera to suppress interfering signals, primarily scattered laser light. The total range covered by these measurements is ~145-200 cm.

Since a 2-D detector was utilized for these measurements, imaging of the fluorescence signal was carried out. The laser beam was shaped into a sheet with a height of ~5mm. Focus of the sheet was positioned at the center of the flame and the width of the beam at the focus was around 0.5 mm. Figure 13(a) displays an example of a fluorescence image obtained at a distance of approximately 1.5 meter, while a horizontal cross section obtained by vertical integration of the signal can be seen in Fig. 13(b). The difference in range of the probe volume is rather small in this case and therefore the fact that the fluorescence signal is collected from different ranges has not been compensated for. To obtain quantitative results, especially over longer distance, a compensation with a theoretical or experimental reference has to be carried out.

For comparison, another ICCD camera (PI-MAX2) was monitoring the fluorescence at a 90-degree-angle relative to the direction of the laser beam at a distance of 40 cm, and an image recorded with this camera, together with its horizontal cross section, can be seen in

Optics EXPRESS

Figs. 13(c) and 13(d), respectively. The two measurements were recorded the same day but not simultaneously. The two images [Figs. 13(a) and 13(c)] as well as the corresponding horizontal cross sections [Figs. 13(b) and 13(d)] agree rather well. The resolution of the close-up detection is somewhat better, with a 10-90% slope width of 1.5 mm compared to 2.6 mm for the remote detection. The effect of the lower resolution is mostly visible in the center of the flame where the dip gets less pronounced for the remote detection. It is important to emphasize that the resolution of the Lidar measurement is specific for this particular distance and beam size. The small fluctuations in the center of the signal are due to imperfections in the porous plug of the burner and the differences in these fluctuations for the stand-off and close-up cases are partly due to the instability of the indium seeding of the flame. This result demonstrates that LIF can be reliably utilized for combustion diagnostics with Scheimpflug Lidar, not only for probing along a line, but also for imaging.

The peaks in fluorescence signal at the edges of the flame are due to an outer reaction zone, where the product gas reacts with the oxygen in the air. Decomposition of indium species and radicals in this reactive zone will increase the number of indium atoms and a high signal is obtained. This profile becomes flatter for flames with less fuel-rich mixing ratios [37]. The lower temperatures at the edges may also contribute to this effect since the number density is higher.

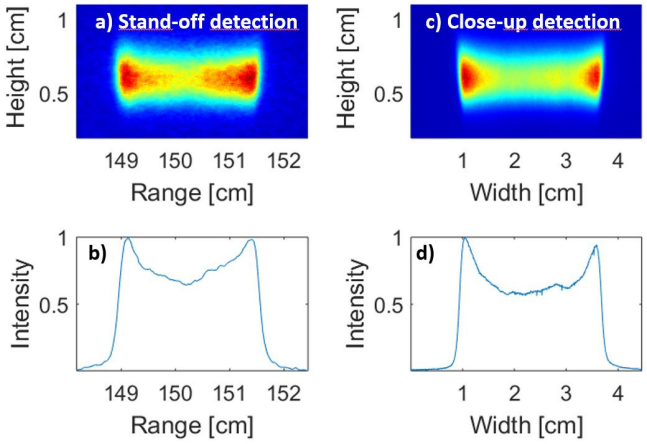

Fig. 13. (a) 2-D Scheimpflug Lidar signal of a laser sheet with a height of 5 mm. The detected indium fluorescence had a wavelength of 451.17 nm. (b) A cross section of the Lidar signal in (a). (c) ICCD image of the fluorescence signal acquired with collection at 90° angle relative to the laser beam path. (d) Cross section of the signal in (c). The signals for both (a) and (b) are an average of 200 images with an exposure time of 8 ms.

5. Conclusions/outlook

A CW-Lidar system has been developed with a particular focus on combustion diagnostics. The system is based on triangulation, rather than the time-of-flight as in conventional Lidar, to attain range information. By positioning the detector, collection optics, and the laser beam in a configuration that fulfils the Scheimpflug principle, infinite focal depth can be obtained and the laser beam can thus be sharply imaged onto the detector.

A theoretical characterization of the near-field Scheimpflug Lidar method with respect to attainable range and range resolution has been made. Simulations corresponding to different setups, which fulfill the Scheimpflug and Hinge conditions, demonstrate the non-linearity of the range scale and that the technique has a trade-off between desired range interval and range resolution. An important point to make is that the non-linear range resolution can, for gas phase measurements, be advantageous, since the decrease of backscattering signal with range

Optics EXPRESS

get compensated for, to a large degree, by the increasing size of the pixel foot print, and the dynamic range of the detector can thus be utilized more efficiently than it could using e.g. time-of-flight Lidar. Exactly how the increasing pixel foot print affects the resulting signal at a specific range is determined by the size and shape of the laser beam profile as well as the degree of overlap between the field-of-view of the detector and the laser beam [25,27,29]. The simulations clearly show that the width of the laser beam has significant impact on the obtained range resolution, and subsequently also the signal. The experimental results confirm the impact of the finite laser beam width on the resolution. A wider laser beam will deteriorate the range resolution. It is therefore vital to keep the beam width as small as possible if high range resolution is essential. Consequently, it is also possible to adjust the range resolution curve by shaping the beam, e.g. if a linear range curve is desired the beam can be shaped in such a way that the decrease in beam width matches the declining resolution due to increasing distance from the system [25,27].

This study also investigates possible ways to decrease the size of the required optical access by changing the focal length of the collection optics, since different f will result in different distances between the laser beam and collection optics. This also turns out to be a trade-off between the range interval, the range resolution, and the size of the required optical access.

The present portable Lidar system has been successfully demonstrated for a number of important diagnostics in combustion applications, including remote LIF and Rayleigh scattering measurements. The latter was also used to obtain remote temperature profiles in non-sooting flames with high range and time resolution. The demonstration of remote LIF measurements using Lidar opens up for remote 2-D temperature measurements using two-line atomic fluorescence (TLAF), in which two single-mode lasers emitting at different wavelengths probe the population of two different energy levels in a seeded atom, for example indium, as described in [37]. It is also shown that the method has the ability to monitor particle distributions with high spatial and temporal resolution. Such particle distributions could provide crucial information for researchers in combustion and other environmental research.

CMOS sensors with up to 80 kHz line-scan rate are now commercially available, and with such a detector implemented into the Lidar system the temporal resolution could be improved a factor 20 compared with the highest resolution demonstrated in this work. Although, only CW-diode laser has been utilized so far, the setup is not limited to this type of lasers, and in principle the laser can be chosen based on the demands of the application in question. We are planning to demonstrate Scheimpflug Lidar using a pulsed, high power laser system in combination with an ICCD camera, which would enable suppression of strong background radiation through time gating. Since high background levels are anticipated in harsh combustion environments, this type of configuration could potentially be needed in some industrial applications. It is anticipated that Scheimpflug Lidar will provide a useful and versatile tool for combustion research, not only for fundamental studies, but in particular for field campaigns at industrial sites.

Funding

Swedish Energy Agency (Energimyndigheten) KC and Gen CECOST (225383, 389131); The European Research Council through the advanced grant TUCLA (669466); Knut and Alice Wallenberg foundation (2013.0036, 2015.0294)

Acknowledgments

We are thankful for the technical assistance and advices by Jesper Borggren, regarding the indium fluorescence experiments.